

Spinal Basis of Direction Control during Locomotion in Larval Zebrafish

Michael Jay,¹ Malcolm A. MacIver,^{1,2,3} and David L. McLean¹

¹Department of Neurobiology, Weinberg College of Arts and Sciences, Northwestern University, Evanston, Illinois 60208, ²Department of Biomedical Engineering, McCormick School of Engineering, Northwestern University, Evanston, Illinois 60208, and ³Department of Mechanical Engineering, McCormick School of Engineering, Northwestern University, Evanston, Illinois 60208

Navigation requires steering and propulsion, but how spinal circuits contribute to direction control during ongoing locomotion is not well understood. Here, we use drifting vertical gratings to evoke directed “fictive” swimming in intact but immobilized larval zebrafish while performing electrophysiological recordings from spinal neurons. We find that directed swimming involves unilateral changes in the duration of motor output and increased recruitment of motor neurons, without impacting the timing of spiking across or along the body. Voltage-clamp recordings from motor neurons reveal increases in phasic excitation and inhibition on the side of the turn. Current-clamp recordings from premotor interneurons that provide phasic excitation or inhibition reveal two types of recruitment patterns. A direction-agnostic pattern with balanced recruitment on the turning and nonturning sides is primarily observed in excitatory V2a neurons with ipsilateral descending axons, while a direction-sensitive pattern with preferential recruitment on the turning side is dominated by V2a neurons with ipsilateral bifurcating axons. Inhibitory V1 neurons are also divided into direction-sensitive and direction-agnostic subsets, although there is no detectable morphologic distinction. Our findings support the modular control of steering and propulsion by spinal premotor circuits, where recruitment of distinct subsets of excitatory and inhibitory interneurons provide adjustments in direction while on the move.

Key words: interneurons; motor neurons; optomotor; spinal cord; swimming; turning

Significance Statement

Spinal circuits play an essential role in coordinating movements during locomotion. However, it is unclear how they participate in adjustments in direction that do not interfere with coordination. Here we have developed a system using larval zebrafish that allows us to directly record electrical signals from spinal neurons during “fictive” swimming guided by visual cues. We find there are subsets of spinal interneurons for coordination and others that drive unilateral asymmetries in motor neuron recruitment for direction control. Our findings suggest a modular organization of spinal premotor circuits that enables uninterrupted adjustments in direction during ongoing locomotion.

Introduction

Animal navigation requires adjustments in orientation during locomotion. In vertebrates, descending command systems relay directional information to the spinal cord, where premotor spinal interneurons coordinate movements across and along the body (Goulding, 2009; Roberts et al., 2010; Kiehn, 2016; Grillner and El Manira, 2020). Traditionally, electrophysiological studies

of spinal interneurons necessitate reduced preparations, which has limited our understanding of their contribution to direction control. More recent work assessing the connectivity of molecularly defined circuits suggests that spinal interneurons are subdivided based on their control of motor neuron recruitment or coordination (Dougherty et al., 2013; Ha and Dougherty, 2018; Song et al., 2018; Menelaou and McLean, 2019). Modular control systems for adjusting the intensity of limb/trunk movements and coordinating the timing of rhythmic movements would be useful for fine adjustments in the direction of forward travel during navigation. However, this idea has been difficult to test given the challenge of evoking changes in orientation while recording from spinal neurons during locomotion.

To address this issue, we have developed a paradigm that allows us to electrophysiologically record from spinal motor neurons and interneurons during visually driven “fictive” swimming in intact larval zebrafish. Like all mobile, visual creatures, larval

Received Mar. 31, 2022; revised Apr. 14, 2023; accepted Apr. 18, 2023.

Author contributions: M.J., M.A.M., and D.L.M. designed research; M.J. performed research; M.J. analyzed data; M.J. and D.L.M. wrote the paper.

Support was provided by National Science Foundation Grant IOS 1456830; and National Institutes of Health Grants U19-NS-104653, R21-NS125187, and R21-NS-125207. We thank Rachel Gocker and Amber Chiodini for fish care, and Moneeza Agha and James Murray for discussions and comments on the manuscript.

The authors declare no competing financial interests.

Correspondence should be addressed to David L. McLean at david-mclean@northwestern.edu.

<https://doi.org/10.1523/JNEUROSCI.0703-22.2023>

Copyright © 2023 the authors

zebrafish use patterns of light to guide their movements. For example, larvae will align themselves to swim in the direction of drifting visual gratings during the optomotor response (Neuhauss et al., 1999; Portugues and Engert, 2011), migrate toward an optimally lit region during phototaxis (Burgess et al., 2010; Chen and Engert, 2014), pursue small prey items (McElligott and O'Malley, 2005; Bianco et al., 2011; Patterson et al., 2013; Trivedi and Bollmann, 2013), and avoid large predators (Temizer et al., 2015; Dunn et al., 2016; Bhattacharyya et al., 2017). In all of these visuomotor behaviors, larval zebrafish adjust the direction of travel using turns and asymmetric “directed” swimming movements.

We find that during directed optomotor responses there is a unilateral increase in the fraction of the swim cycle occupied by motor bursts, accompanied by an increase in motor neuron recruitment probability. This occurs without impacting the timing of spikes, or the left–right alternation or head–tail phase lag of motor bursts, meaning adjustments in movement intensity can be achieved without impacting timing. We then perform recordings from canonical spinal interneuron populations implicated in motor neuron recruitment and coordination (Kimura et al., 2006; Ausborn et al., 2012; Song et al., 2018, 2020; Kimura and Higashijima, 2019; Menelaou and McLean, 2019; Guan et al., 2021; Sengupta et al., 2021), which reveal turn direction-sensitive and direction-agnostic subsets consistent with modular control of intensity and timing.

Collectively, our findings support the modular control of locomotion, where turn direction-sensitive V2a and V1 subsets can modulate motor neuron recruitment unilaterally to adjust direction and direction-agnostic V2a and V1 subsets can maintain segmental coordination of rhythmic movements bilaterally to ensure uninterrupted forward progress.

Materials and Methods

Animals. Experiments were performed on free-swimming 5–6 d postfertilization wild-type, enhancer trap $\text{parg}^{\text{MNET2}}::\text{GFP}$ (Balciunas et al., 2004), $\text{Tg}[\text{EN1:GAL4;UAS:GFP}]$ (Higashijima et al., 2004a), and $\text{Tg}[\text{CHX10:GFP}]$ (Kimura et al., 2006) zebrafish (*Danio rerio*) larvae obtained from adults housed in an in-house facility (Aquatic Habitats). Zebrafish were maintained at 28.5°C in system water on a 14 h/10 h light/dark cycle before experiments. All procedures described conform to National Institutes of Health guidelines regarding animal experimentation and were approved by the Northwestern University Institutional Animal Care and Use Committee (IS00019359 and IS00019319). Experiments were performed at room temperature (~24°C).

Electrophysiology. Zebrafish larvae were first immobilized in an extracellular solution (in mM: 134 NaCl, 2.9 KCl, 1.2 MgCl_2 , 2.1 CaCl_2 , 10 HEPES, and 10 glucose, adjusted to pH 7.8 with NaOH) containing 1 mg/ml α -bungarotoxin (Sigma-Aldrich) and then transferred to a Sylgard-lined glass-bottomed dish, 35 mm in diameter (World Precision Instruments), containing extracellular solution. Electrolytically sharpened tungsten pins were placed through the notochord, and the larvae were positioned 8–10 mm from the perimeter of the dish. To reduce the potential contribution of vestibular afferents to fictive motor output (Bagnall and McLean, 2014) and enable appropriate delivery of visual stimuli, the head was rotated upright and kept in place using tungsten pins (Fig. 1A). For recordings from spinal neurons, the skin along the trunk was removed and musculature lateral to the spinal cord was carefully aspirated using a broken glass pipette mounted on a micromanipulator. Dissection was typically limited to one to two hemisomites, particularly when recording from motor neurons, to permit visualization of axonal projections into the musculature postrecording.

Whole-cell patch-clamp electrodes made from standard-wall 1-mm-outer diameter borosilicate glass (A-M Systems) were backfilled with a K-gluconate solution (in mM: 125 K-gluconate, 2.5 MgCl_2 , 10 EGTA, 10

HEPES, and 4 $\text{Na}_2\text{-ATP}$, adjusted to pH 7.3 with KOH) for current-clamp recordings, containing 0.1% sulforhodamine-B chloride. For voltage-clamp recordings, electrodes were filled with the following cesium-based solution (in mM): 122 CsMeSO_3 , 0.5 QX314, 1 TEA, 3 MgCl_2 , 10 HEPES, 10 EGTA, and 4 $\text{Na}_2\text{-ATP}$, adjusted to pH 7.3 using CsOH, containing 0.1% sulforhodamine-B chloride. In all whole-cell recordings, a calculated junction potential of 10 mV (K-gluconate solution) or 16 mV (cesium-based solution) were corrected for during analysis. Suction electrodes for recording the activity of peripheral ventral rootlets were fashioned from these electrodes by cleanly breaking the tips to diameters of 20–50 μm . A microforge (model MF-830, Narishige) was used to heat polish and bend the tip to compensate for the approach angle (~20°), which improved the contact between the opening of the electrode and the muscle cleft.

All electrophysiological recordings were acquired using a Multiclamp 700B Amplifier, a Digidata series 1322A Digitizer, and pClamp software (Molecular Devices). Standard corrections for bridge balance and electrode capacitance were applied in current-clamp mode, and series compensation (60–70%) was applied in voltage-clamp mode. Electrical signals from spinal cells were filtered at 100 kHz and digitized at 100 kHz at a gain of 10 (feedback resistor, 500 M Ω). Extracellular signals from the ventral rootlets were recorded at a gain of 1000 with low-frequency and high-frequency cutoffs set at 100 and 4000 Hz, respectively.

Except during a subset of dual ventral rootlet activity recordings, ventral rootlet activity was recorded on the ipsilateral (ipsi) side of the targeted cell. For whole-cell recordings, electrodes were mounted on motorized micromanipulators (model MP-225, Sutter Instruments) and advanced into the spinal cord under positive pressure (~10 mmHg) near to the target cell. The electrode was quickly brought into contact with the targeted cell soma, positive pressure was removed, and a gigaohm seal was obtained either spontaneously or through the application of a small amount of negative pressure. To confirm that the recruitment of spinal neurons was not affected by the composition of the current-clamp K-gluconate solution, cell-attached recruitment data were obtained during visual stimuli in a subset of experiments. Under these conditions, the electrode was held at a potential where the holding current was 0 pA to minimize inadvertently affecting the firing properties of the cell (Perkins, 2006). Since recruitment patterns were not significantly different between cell-attached and whole-cell methods, data were pooled. To gain whole-cell access, small pulses of negative pressure were applied. Shortly after whole-cell configuration was achieved, spike capacity was assessed using the pClamp membrane test panel. To accurately determine input resistance offline, a series of hyperpolarizing square current steps were injected to calculate input resistance according to Ohm's law. To isolate excitatory or inhibitory currents in voltage clamp, cells were held at –65 or –20 mV, respectively. Ventral rootlet electrodes were placed onto the vertical myoseptum near to the recording site (1.6 ± 0.06 somites caudal to cell body; $n = 138$ larvae) after a gigaohm seal with the targeted spinal neuron was obtained. Constant negative pressure (approximately –10 mmHg) was then applied to the large-diameter electrode to help maintain contact with the musculature for the duration of the experiment.

Imaging. After performing electrophysiological recordings, the identity of targeted cells was confirmed by switching to an epifluorescent light source and examining GFP expression and axon projection patterns of the targeted neurons. Targeted neurons would fluoresce because the patch solution also included a small amount of sulforhodamine-B chloride. Images of cells were captured using a cooled charge-coupled device camera (Rolera-XR, Q-Imaging) and a rhodamine filter set. To determine soma location and morphology, we collected a series of images at higher magnification, gradually focusing down from the muscle to the far side of the spinal cord. In both cases, we captured fluorescent and differential interference contrast images. Dorsoventral soma position was based on an average of three measurements of the middle of the cell body normalized to an average of three measurements of the dorsal-most and ventral-most boundaries of the spinal cord using ImageJ. To be included in the analysis, the borders of the spinal cord had to be obvious and undamaged. Reconstructions of neurons are based on a series of fluorescent images and were traced using Adobe Photoshop using

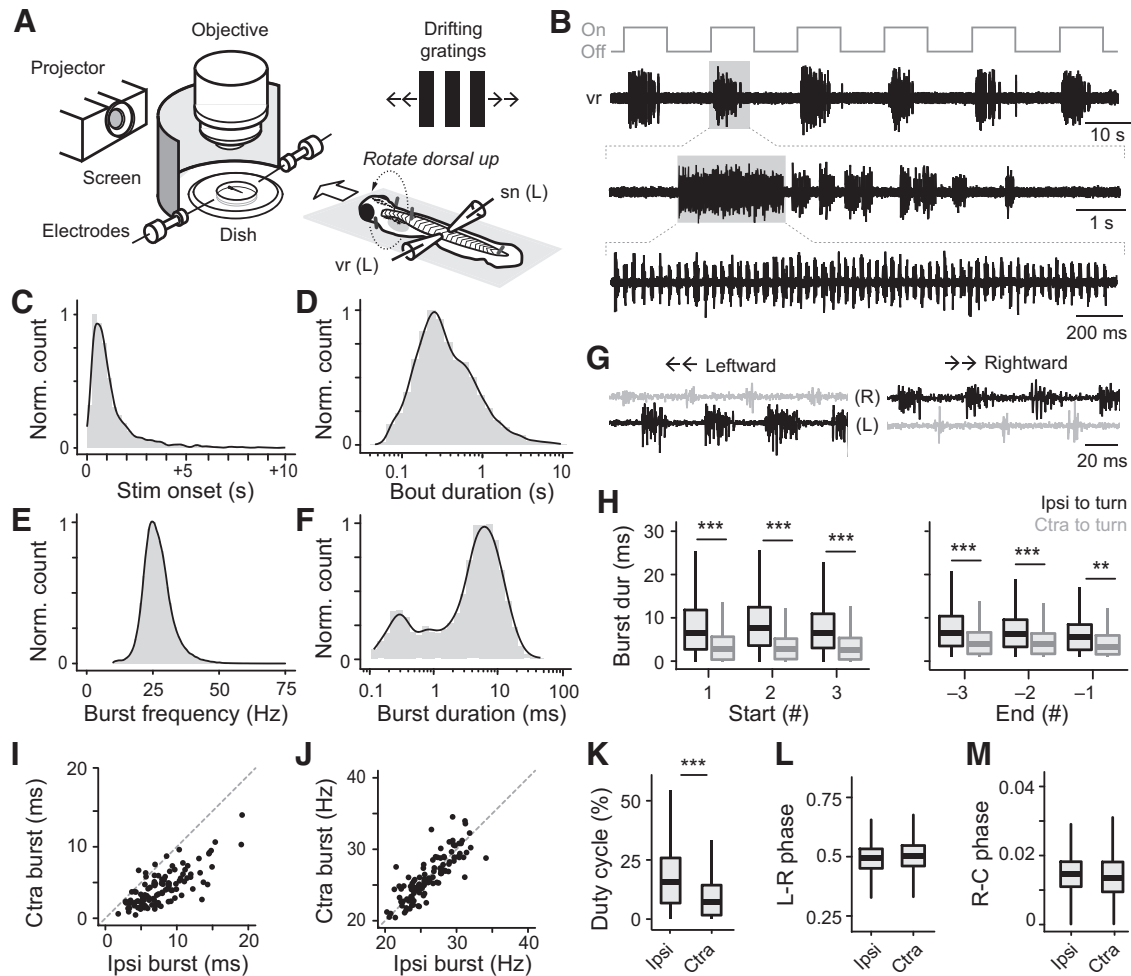


Figure 1. Fictive motor patterns during optomotor responses. **A**, Schematic of setup used to present drifting gratings and simultaneously record motor activity from ventral rootlets (vrs) and spinal neurons (sns). Except for ventral rootlet pairs, all recordings were done on the left side of the body (L). The head was rotated dorsal side up to decrease the likelihood of vestibular-mediated responses and enable delivery of visual stimuli to both eyes. **B**, Example fictive swim episodes (black) recorded from a vr during drifting grating stimuli. Gray line indicates when the stimulus was applied. Each stimulus presentation (trial) reliably evoked fictive swimming (top trace), which was composed of several bouts (middle trace). Each bout contained rhythmic bursts of motor activity (bottom trace). Gray-shaded boxes indicate regions of expansion. **C**, Normalized histogram of the onset of the first swim episode relative to stimulus onset ($n = 1411$ bouts from 124 fish). Here and below, the black line indicates a smoothed density estimate. **D**, Normalized (Norm.) histogram of bout duration during optomotor responses ($n = 8590$ bouts from 124 fish). **E**, Normalized histogram of burst frequency during optomotor responses ($n = 179,220$ bursts from 124 fish). **F**, Normalized histogram of burst durations during optomotor responses ($n = 179,220$ bursts from 124 fish). **G**, Excerpts of leftward (left) and rightward (right) fictive motor activity recorded simultaneously from left (L) and right (R) ventral rootlets during an optomotor response. Note the longer burst durations ipsilateral to turn direction, compared with burst durations contralateral to turn direction. **H**, Box-and-whisker plots of burst duration for the first three bursts (left) and last three (right) cycles within optomotor response swim bouts. Significant differences in burst duration were observed between ipsilateral and contralateral turns for the first three bursts of all bouts (Wilcoxon rank-sum test; Burst 1: $W = 8914709$, $p < 0.001$; Burst 2: $W = 9566484$, $p < 0.001$; Burst 3: $W = 8002631$, $p < 0.001$) and the last three bursts of all bouts (Burst -3: $W = 2932355$, $p < 0.001$; Burst -2: $W = 2859354$, $p < 0.001$; Burst -1: $W = 2818181$, $p < 0.001$). **I**, Scatter plot of mean burst duration (ms) during ipsilateral gratings (Ipsi burst) versus mean burst duration during contralateral gratings (Ctra burst; $n = 114$ fish). Dashed line indicates unity. **J**, Scatter plot of mean burst frequency (Hz) during ipsilateral gratings (Ipsi burst) versus mean burst frequency during contralateral gratings (Ctra burst; $n = 114$ fish). Dashed line indicates unity. **K**, Box-and-whisker plots of duty cycle during optomotor responses. Significant differences between ipsilateral and contralateral optomotor responses were observed (Wilcoxon rank-sum test, $W = 11293$, $p < 0.001$). **L**, Box-and-whisker plot of left-right alternating phase. No significant differences were observed in left-right alternation (Wilcoxon rank-sum test, $W = 37$, $p > 0.05$). **M**, Box-and-whisker plot of rostrocaudal phase during pooled optomotor. No significant differences were observed (Wilcoxon rank-sum test, $W = 56$, $p > 0.05$). Asterisks indicate significance level; * $p < 0.05$; ** $p < 0.001$; *** $p < 0.0001$.

z-compression stacks made in ImageJ. Cell identity was confirmed using a combination of soma size, position, GFP expression, axonal projections, and intrinsic electrophysiological properties.

Visual assay. Drifting gratings were generated with Psychtoolbox (Kleiner et al., 2007) within MATLAB and directionality was randomly determined. Open-loop drifting gratings were presented for 10 s in 20 s intervals and moved at a rate of 10 mm/s to the left or right, to evoke leftward and rightward turns, respectively (Roeser and Baier, 2003). Visual stimuli were projected with a 450 lumen portable LED projector (model M115HD, Dell) onto a diffusive filter placed along the perimeter of the recording chamber. Larvae were positioned such that they were orientated toward the center of the screen (Fig. 1A).

Analysis. For analysis, 9–10 trials [ipsi = 9.8 ± 0.6 ; contralateral (cra) = 9.4 ± 0.6 trials, Wilcoxon rank-sum test, $p > 0.05$] comprising 20–25 bouts of fictive swimming activity (ipsi = 23.5 ± 2.1 ; cra = 23.0 ± 2.1 bouts; Wilcoxon rank-sum test, $p > 0.05$) were recorded per larva, and data from all trials was pooled. Electrophysiological data were analyzed in DataView (version 11.12.2), MATLAB (version 2016b; MathWorks), and R (version 4.1.2). DataView was first used to extract the timing of visual stimuli, ventral rootlet activity, and action potentials in current-clamp or cell-attached mode. Action potentials were identified by threshold detection on the raw signal in cell-attached mode or by taking the first-order differential of the raw electrophysiological signal and then using threshold detection in the current-clamp configuration. Instantaneous frequency was defined as the reciprocal of the interval in

seconds between successive action potentials. MATLAB was used to determine the timing of action potentials or voltage-clamp activity relative to ventral rootlet activity. EPSCs or IPSCs were identified using the *findpeaks* function in MATLAB. Finally, R was used to visualize data and perform statistical analyses. The timing of action potentials and voltage-clamp data was measured relative to the center of ventral rootlet activity, and phase values were calculated with respect to the center of bursts. In all polar phase plots, a value of 0 corresponds to the center of the burst and 1 corresponds to the center of the proceeding burst. Direction-sensitive neurons were defined as neurons having a ctra/ipsi 1:3 ratio in recruitment probability.

Before testing for statistical significance, all data were first tested for normality to determine whether parametric or nonparametric tests were appropriate. Comparisons between two groups were performed using Wilcoxon rank-sum or signed-rank tests for non-normal data or paired or unpaired *t* test for normal data. For circular data, Watson's two-sample test of homogeneity was used to determine whether phase values from two conditions were significantly different from each other. Mean values \pm SE are reported within the text, unless stated otherwise. Statistical significance is reported as follows: * $p < 0.05$; ** $p < 0.01$; *** $p < 0.001$.

Results

Fictive motor patterns in response to drifting vertical gratings reflect directed swimming

To begin, we designed a system to deliver visual stimuli while performing simultaneous whole-cell recordings from neurons in the spinal cord and extracellular recordings of ventral rootlets containing peripheral motor nerves in a chemically immobilized preparation capable of producing fictive motor output (Fig. 1A). To evoke directionally asymmetric swim episodes, we used drifting vertical square-wave gratings to evoke the optomotor response, which is characterized by reorientation in the direction of the drifting gratings (Neuhauss et al., 1999; Portugues and Engert, 2011). The protocol for measuring directed optomotor responses comprised trials lasting 10 s with randomly selected leftward or rightward directionality and a fixed speed of 10 mm/s. Intertrial durations were 10 s, during which time the gratings were stationary. Our experimental paradigm operated in an open-loop configuration, so we expected fish to continuously engage in directed swimming, as opposed to closed-loop or free swimming where motor output alters optic flow. During fictive optomotor responses (Fig. 1B), intermittent "bouts" of swimming were reliably evoked in $89.1 \pm 1.17\%$ of trials (median, 100%; $n = 129$ fish), and each stimulus presentation evoked multiple swim bouts (Fig. 1B, middle). Swim bouts began shortly after stimulus onset (Fig. 1C) and were typically 300 ms in duration but could last the entire duration of the trial (Fig. 1D). The high reliability, latency, and maintenance of swimming activity in response to drifting stimuli is consistent with optomotor responses observed under more naturalistic conditions (Neuhauss et al., 1999; Portugues and Engert, 2011).

To determine whether leftward or rightward drifting gratings were evoking the asymmetric motor output required for directed swimming, we examined individual motor bursts within bouts (Fig. 1B, bottom). During fictive optomotor responses, burst frequencies rarely exceeded 30 Hz (Fig. 1E), which is the low end of the full dynamic range in larvae (Buss and Drapeau, 2001; McLean and Fetcho, 2009; Eklöf-Ljunggren et al., 2012), and burst durations rarely exceeded 10 ms (Fig. 1F). The most obvious impact of drifting stimuli was on the duration of motor bursts (Fig. 1G), which were significantly longer on the turning side at both the start and end of the bout (Fig. 1H). Indeed,

with few exceptions ($n = 5$ of 114 larvae), bursts were longer in duration on the turning side when averaged across all bouts and trials (ipsi = 7.61 ± 0.04 ms; ctra = 3.68 ± 0.03 ms; $n = 114$ larvae; Fig. 1J). In contrast, there was no significant modulation of swim frequency related to turn direction (Fig. 1J). The increase in burst durations and consistent frequency meant that the "duty cycle" (percentage of the swim cycle occupied by motor bursts) significantly increased on the turning side (Fig. 1K). Consistent with a lack of impact of turn direction on swim frequency, we also observed no significant impact on the timing of motor bursts across the body or along it, as measured by the phase of left-right alternation (Fig. 1L) and the head-tail phase lag per segment (Fig. 1M), respectively.

In sum, quantifiable features of fictive optomotor responses are consistent with real optomotor responses in freely moving and partially restrained fish (Orger et al., 2008; Severi et al., 2014), supporting the use of our system to explore the spinal basis of directed swimming. These observations also suggest that larvae modulate the direction of forward travel by increasing the proportion of the cycle occupied by motor activity, without interfering with coordination across or along the body.

Increases in motor neuron recruitment during directed swimming

Next, to determine the sources of increased motor output observed in our ventral rootlet recordings, we performed whole-cell current-clamp recordings from axial motor neurons targeted blindly in wild-type larvae or in *par^{MNET2}:GFP* larvae based on fluorescence (Balciunas et al., 2004). Recordings were performed from identified motor units (Myers et al., 1986; Bello-Rojas et al., 2019)—specifically "fast" p-type ($n = 63$) and m-type ($n = 23$) units that are defined by their innervation of deeper fast twitch muscle fibers and "slow" ms-type ($n = 3$) and s-type ($n = 8$) units that are defined by their innervation of superficial slow muscle (Fig. 2A). Recordings also included unidentified secondary motor neurons where cell-attached recordings in *par^{MNET2}:GFP* larvae did not progress to whole-cell recordings ($n = 11$) or the axons were too fine to be labeled with dye to track muscle innervation ($n = 14$). We classified these as "slow" units for purposes of analysis because their more ventral distributions, higher-input resistances, relatively small somata, and fine caliber axons were consistent with s-type motor neurons (Menelaou and McLean, 2012; Bello-Rojas et al., 2019).

Fast motor units recruited during drifting stimuli had lower input resistances (Fig. 2B) than recruited slow motor units, consistent with previous reports (Menelaou and McLean, 2012; Bello-Rojas et al., 2019), although we found no corresponding differences in soma position (Fig. 2C). Recordings revealed the following three major categories of response: (1) neurons were not recruited but exhibited an increase in rhythmic subthreshold drive on the turning side (Fig. 2D, top); (2) motor neurons were recruited more reliably on the turning side (Fig. 2D, middle); and (3) motor neurons were largely agnostic to turn direction (Fig. 2D, bottom). To further characterize differences in the recruitment of fast and slow motor pools, we plotted recruitment reliability contralateral to the turn versus recruitment reliability ipsilateral to the turn and defined neurons that deviated 33% from unity as direction sensitive (Fig. 2E). In the recruited pool of fast motor neurons, 68% were preferentially active during ipsilateral gratings ($n = 15$ of 22 cells), while the remaining were agnostic to direction (Fig. 2E). Within the recruited pool of slow units there was a comparable proportion of direction-sensitive versus agnostic subsets ($n = 10$ of 15 cells or 67%; Fig. 2E). When

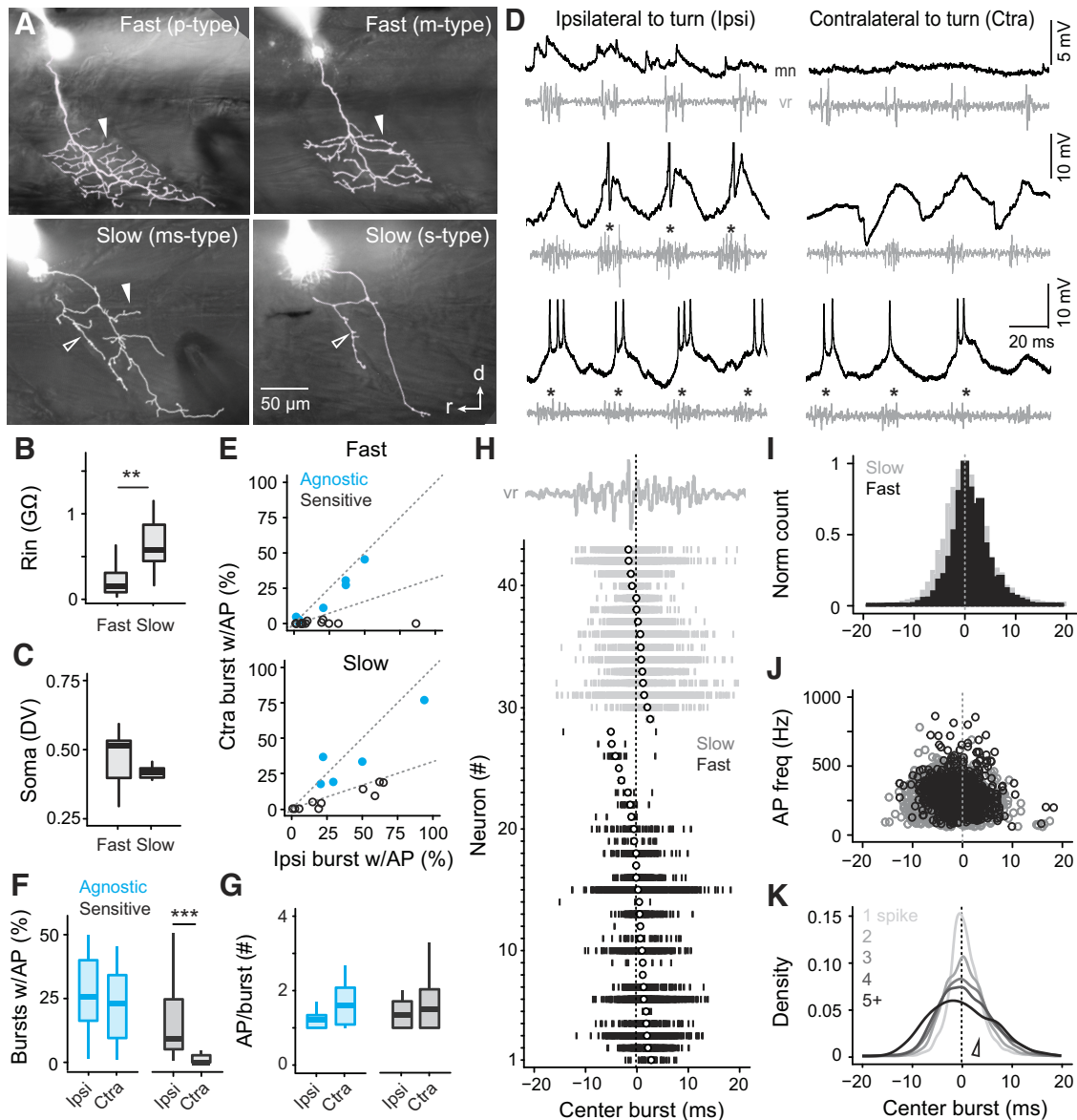


Figure 2. Motor neuron recruitment patterns during directed swimming. **A**, Lateral views of fast (p-type and m-type) and slow (ms-type and s-type) motor neurons. Filled arrowheads indicate medial branches of the peripheral axon in the deeper fast muscle fibers, while open arrowheads indicate septal branches in the superficial slow muscle fibers. Axon reconstructions are superimposed on composite fluorescence/differential interference contrast images collected *post hoc*, which reveal the dye-filled electrode and the chevron-shaped muscle segment. Illustrated motor neurons innervate ventral, hypaxial muscle. d, Dorsal; r, rostral. **B**, Box-and-whisker plots of input resistances (in $G\Omega$) of recruited motor neurons (fast, $n = 27$; slow, $n = 18$). Significant differences were observed between fast and slow motor neuron input resistances (Wilcoxon rank-sum test, $W = 32$, $p < 0.01$). **C**, Box-and-whisker plots of dorsoventral (DV) somata locations of recruited motor neurons (fast, $n = 34$; slow, $n = 18$); 0 and 1 signify the ventral and dorsal boundaries, respectively. No significant difference was observed between fast and slow soma DV positions (Wilcoxon rank-sum test, $W = 124$, $p > 0.05$). **D**, Excerpts of current-clamp recordings from three different motor neurons (mns) with simultaneous ventral rootlet (vr) recordings during ipsilateral (left) and contralateral (right) gratings. Action potentials are truncated to reveal underlying synaptic drive. Motor bursts accompanied by motor neuron recruitment are demarcated by asterisks. Resting membrane potentials: -70 mV (top), -65 mV (middle), and -65 mV (bottom). **E**, Scatter plot of average recruitment probability, defined as number of motor bursts with action potentials (APs) over the total number of observed motor bursts, during ipsilateral (Ipsi burst w/AP) and contralateral (Ctr burst w/AP) turns for direction-sensitive (open black circle) and direction-agnostic (blue circle) motor neurons. Dashed lines indicate unity and the boundary for distinguishing agnostic and direction-sensitive neurons. **F**, Box-and-whisker plots of recruitment as the percentage of motor bursts with spikes for agnostic (blue) and direction-sensitive (black) motor neurons during ipsilateral and contralateral gratings. Significant differences were observed between ipsilateral and contralateral gratings for direction-sensitive motor neurons (Wilcoxon rank-sum test, $W = 74$, $p < 0.001$). No significant difference was observed between ipsilateral and contralateral gratings for agnostic motor neurons (Wilcoxon rank-sum test, $W = 62$, $p > 0.05$). **G**, Box-and-whisker plots of the mean number of action potentials only during cycles in which motor neurons were recruited. No significant differences were observed between ipsilateral and contralateral gratings for direction-agnostic (blue, Wilcoxon rank-sum test, $W = 68$, $p > 0.05$) or direction-sensitive (Wilcoxon rank-sum test, $W = 121$, $p > 0.05$) motor neurons. **H**, Raster plot showing the timing of spikes from all recruited motor neurons (bottom) relative to the center of nearby ventral rootlet activity. Each row represents action potentials (tick marks) from the same motor neuron across all recorded ipsilateral and contralateral trials. Open circles are median values. Fast motor neurons are shaded black ($n = 28$ cells) and slow motor neurons are shaded gray ($n = 15$ cells). Top trace, An example of mn recruitment aligned to the center of nearby ventral rootlet activity. **I**, Normalized histogram of spike timing relative to the center of nearby ventral rootlet activity for all motor neurons, divided into fast (black, $n = 2908$ spikes) and slow (gray, $n = 5309$ spikes) motor neurons. **J**, As in **I**, but spike timing relative to center burst versus instantaneous spike frequency. **K**, As in **I**, but spike densities partitioned by the observed number of spikes per burst. Open arrowhead marks dip in spike densities in the second half of the burst. Asterisks indicate significance level; * $p < 0.05$; ** $p < 0.001$; *** $p < 0.0001$.

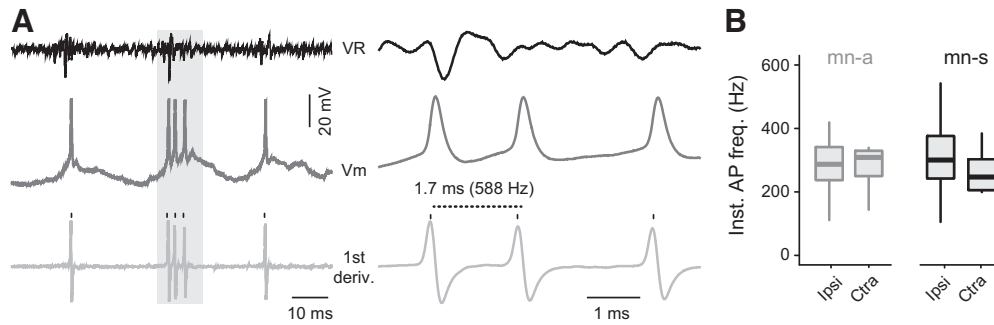


Figure 3. Motor neuron instantaneous spike frequency is not modulated by turn direction. **A**, Method for offline spike detection during fictive optomotor responses. In cell-attached mode, action potentials (APs) were identified by threshold detection of the raw trace. In current-clamp mode, the first-order differential of the intracellular trace was calculated (bottom) and then a threshold was used to detect spikes (black tick marks). Instantaneous frequencies between successive spikes were calculated by taking the reciprocal of the difference in seconds between spikes (dashed line). Gray box indicates a region of expansion (right). **B**, Box-and-whisker plot of instantaneous AP frequency during recruited bursts for direction-agnostic motor neurons (mn-as) and direction-sensitive motor neurons (mn-s; Wilcoxon rank-sum test; fast: $W = 107$, $p > 0.05$; slow: $W = 95$, $p > 0.05$). Deriv., Derivative; Inst., instantaneous; freq., frequency.

fast and slow motor neuron data were pooled, this revealed a significant difference in recruitment probability among direction-sensitive subsets that was not obvious for agnostic neurons (Fig. 2F). Notably, median probabilities per cycle for both direction-sensitive and direction-agnostic pools rarely exceeded 50%, consistent with the low swimming frequencies observed during fictive optomotor responses. Both fast and slow motor units typically fired one to two spikes per cycle; however, we found no significant difference in spike number during recruited cycles related to turn direction among sensitive and agnostic neurons (Fig. 2G). In addition, there was no significant asymmetry in instantaneous firing frequencies per burst related to turning (Fig. 3A,B).

To see how differences in the temporal distribution of spikes could contribute to increases in motor burst durations and duty cycles recorded peripherally, we normalized spike timing to nearby recordings of ventral rootlets (Fig. 2H, top). Since we observed no significant differences in the timing of ventral root signals (Fig. 1J,L,M), we combined spike-timing information from both ipsilateral and contralateral turns. Spike distributions were aligned to the center of the motor burst to limit the impact of burst durations on timing measurements. Individual motor neuron raster plots representing multiple swim cycles per neuron revealed relatively tight distributions of spikes centered on the motor burst (Fig. 2H), with median distributions falling within ± 5 ms of burst center in slow and fast units. These observations were supported by histograms of spike timing, which revealed a symmetrical distribution of spikes and a peak at burst center for both units (Fig. 2I). Notably, slow units were recruited earlier compared with fast units (Fig. 2I), consistent with respective differences in their input resistances. As observed for the peak distributions of spikes, peak spike frequencies were symmetrically distributed around the burst center for all units (Fig. 2J), reaching 800 Hz (Fig. 2J). Plotting the density of spikes according to the number of spikes per burst revealed a relatively symmetrical broadening in spike distribution around center burst as spike numbers increased (Fig. 2K). However, a notch in the trailing half of the burst was apparent at high spike numbers that suggests a sudden drop in spike probability ~ 5 ms after center burst (Fig. 2K, arrowhead). Critically, regardless of whether neurons fired one spike per cycle or many, peak densities were aligned to the center of the motor burst.

These observations demonstrate that directed swimming primarily involves increases in the recruitment of fast and slow motor units, where increased burst durations and duty cycles

observed on the turning side reflect increases in the active pool of motor neurons that generate more spikes per motor burst. While the majority of fast and slow units ($\sim 70\%$) were direction sensitive, increased motor output was achieved by only subtle adjustments in the recruitment probability per cycle ($\sim 25\%$). In addition, the distribution of spikes is consistent with a phasic timing signal that peaks at the center of the motor burst regardless of motor unit identity, number of spikes, or intensity of motor output.

Selective increases of in-phase excitation and inhibition underpin directed swimming

Next, to explore the phasic premotor signals responsible for directed swimming, we performed whole-cell voltage-clamp recordings of EPSCs and IPSCs from fast ($n = 28$) and slow motor neurons ($n = 5$). First, we explored the phasic nature of motor neuron recruitment by normalizing spikes to the center of successive motor bursts, with 0 representing the middle of the cycle and 1 representing the middle of the preceding cycle (Fig. 4A, top). By convention, spikes, EPSCs, and IPSCs are considered “in phase” if they coincide with local motor output on the ipsilateral side and “antiphase” if they coincide with local output on the contralateral side (Fig. 4A, bottom). As expected, this analysis revealed that motor neuron spikes were predominantly distributed in phase with local motor bursts, with median values around burst center (Fig. 4A). Binning and normalizing spikes to phase confirmed that increases in duty cycle were associated with more reliable spiking in motor neurons (Fig. 4B) and no impact on their peak distributions (Fig. 4C, arrow), consistent with a common timing signal.

To see how excitation and inhibition contribute to phasic spiking patterns, we focused on relatively fast EPSCs and IPSCs (Fig. 4D), which likely represent direct premotor synaptic connections based on their respective time courses (Menelaou and McLean, 2019; Kishore et al., 2020). During recordings on the opposite side to the turn (ctra), EPSCs were observed throughout the swim cycle, but with a peak distribution in phase (Figs. 3E, right, 4D, top). On the same side as the turn (ipsi), excitation arriving in phase increased (Figs. 3E, left, 4D, top) without impacting its peak distribution (Fig. 4F). Notably, the polar distribution of EPSCs was statistically insignificant from the polar distribution of spikes (Fig. 4F; Watson’s test, ipsi spikes vs ipsi EPSCs, $U = 0.06$, $p > 0.05$; ctra spikes vs ctra EPSCs, $U = 0.1$, $p > 0.05$), consistent with their role in coordinating spike timing. On the other hand, IPSCs were observed more consistently

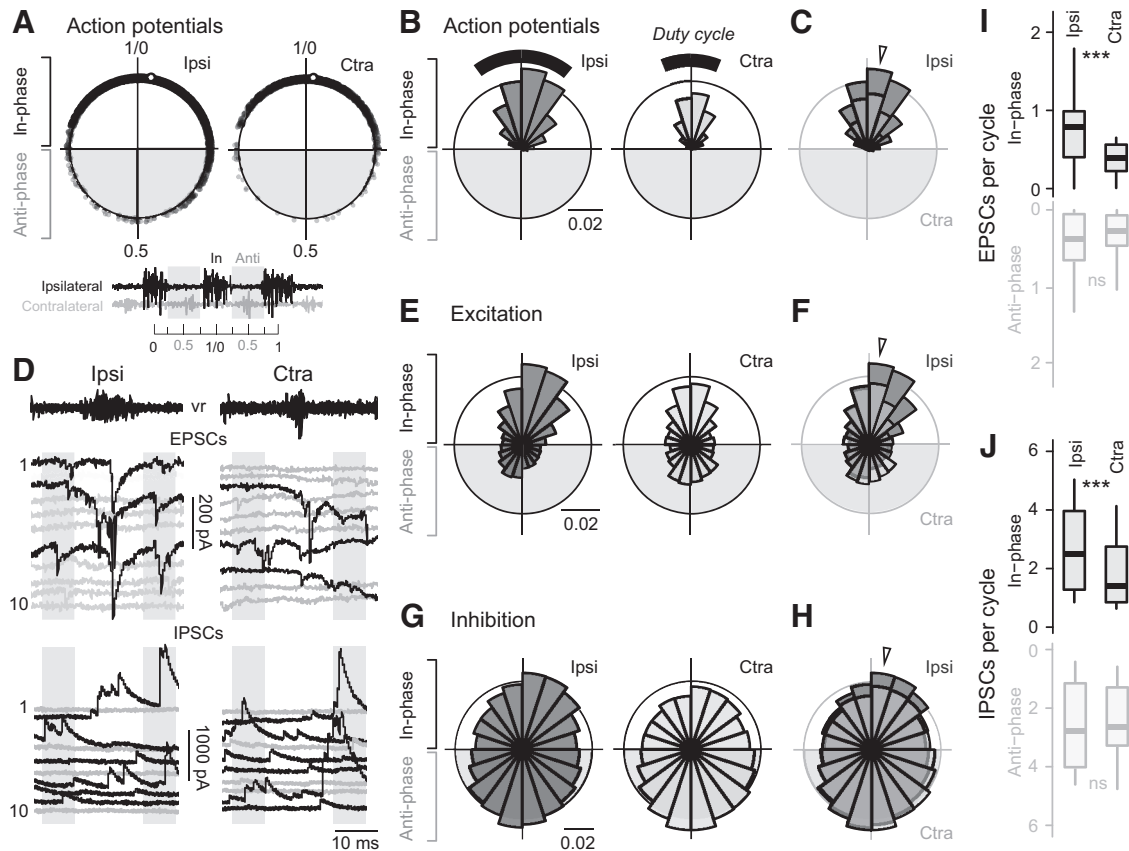


Figure 4. Excitatory and inhibitory inputs to motor neurons during directed swimming. **A**, Top, Polar phase plots of all motor neuron spiking activity normalized to the center of motor bursts (1/0), when recorded on the same side of the turn (Ipsi) and the opposite side (Ctra) during optomotor responses. Bottom, Spikes arriving in phase with ipsilateral motor bursts are distributed between phases 0.75 and 0.25, centered on 0/1, while spikes arriving antiphase with contralateral motor bursts are distributed between phases 0.25 and 0.75, centered on 0.5 (shaded gray areas). **B**, Binned polar plots of recruitment data shown in **A**. Counts are normalized to the total number of cycles recorded in each condition. Black bars indicate the duty cycle. Here and elsewhere, the scale bar for circular plots represents the proportion of total cycles. **C**, Spiking activity during ipsilateral and contralateral turns in **B** overlaid to compare distributions. Arrowhead indicates the peak distribution of spikes. **D**, Excerpts of EPSCs (top) and IPSCs (bottom) aligned to burst center from 10 cycles during ipsilateral (left) and contralateral (right) gratings. Black traces indicate the presence of PSCs, while gray traces indicate the absence of detectable PSCs. Gray areas denote antiphase activity. **E**, Binned polar phase plots of EPSCs recorded from motor neurons ($n = 34$ cells) Ipsi ($n = 17,097$ EPSCs) and Ctra ($n = 9680$ EPSCs) to the turn. Counts are normalized to the total number of EPSCs recorded in each condition. **F**, Overlay of polar plots in **E**. Arrowhead indicates the peak distribution of EPSCs. Ipsilateral and contralateral distributions are not significantly different (Watson's test, $U = 0.12$, $p > 0.05$). **G**, Binned polar-phase plots of IPSCs recorded from motor neurons ($n = 28$ cells) Ipsi ($n = 36,795$ IPSCs) and Ctra ($n = 26,359$ IPSCs) to the turn. Counts are normalized to the total number of IPSCs recorded in each condition. **H**, Overlay of polar plots in **G**. Arrowhead indicates peak distribution of IPSCs. Ipsilateral and contralateral distributions are not significantly different (Watson's test, $U = 0.06$, $p > 0.05$). **I**, Box plots of the number of in-phase (black) and antiphase (gray) EPSCs per cycle across all recorded cycles. Significant differences were observed between ipsilateral and contralateral turns for in-phase (Wilcoxon rank-sum test, $V = 231$, $p < 0.001$) but not for antiphase EPSC counts phase (Wilcoxon rank-sum test, $V = 117$, $p > 0.05$). **J**, Box plots of the number of in-phase (black) and antiphase (gray) IPSCs per cycle across all recorded cycles. Significant differences were observed between ipsilateral and contralateral turns for in-phase (Wilcoxon rank-sum test, $V = 78$, $p < 0.001$), but not antiphase, IPSC counts phase (Wilcoxon rank-sum test, $V = 40$, $p > 0.05$). Asterisks indicate significance level; * $p < 0.05$; ** $p < 0.01$; *** $p < 0.001$.

throughout the swim cycle (Figs. 3G, 4D, bottom), although there did appear to be an increase in inhibition arriving in phase on the turning side (Fig. 4H).

To better quantify these observations, we examined the normalized number of PSCs in phase and antiphase per cycle, for both inhibition and excitation. For excitation, more EPSCs were consistently observed in phase per cycle during ipsilateral turns than contralateral turns for most motor neurons ($n = 28$ of 34 neurons). Analysis of these neurons revealed a significant increase in phase, with no change in antiphase excitation (Fig. 4I). Note that because EPSCs were not observed in every swim cycle (Fig. 4D, top), median values rarely exceeded 1 per cycle. In the remaining neurons, we found no significant change in either in phase (Wilcoxon rank-sum test, $W = 11$, $p > 0.05$) or antiphase (Wilcoxon rank-sum test, $W = 5$, $p > 0.05$) excitation. For inhibition, in 14 of 28 neurons more IPSCs were observed in phase during ipsilateral turns, with no significant corresponding change in antiphase IPSCs (Fig. 4J). In the remaining

cells, there was no significant difference in either in-phase (Wilcoxon rank-sum test, $W = 68$, $p > 0.05$) or antiphase (Wilcoxon rank-sum test, $W = 57$, $p > 0.05$) inhibition.

These observations are consistent with a selective increase in both ipsilateral excitation and inhibition on the turning side during directed swimming that can alter motor neuron activity in direction-sensitive subsets without impacting the timing of spikes.

V2a neurons are divided into turn direction-sensitive and direction-agnostic subsets

According to canonical models of axial swimming circuits (Roberts et al., 2010; Grillner and El Manira, 2020), rhythmic EPSCs and IPSCs arriving in phase coincident with local motor activity arise from local, ipsilateral sources. We began by examining Chx10-labeled V2a interneuron properties since these cells are a major source of ipsilateral premotor excitation. Spinal V2a neurons in both larval and adult zebrafish are divided into two

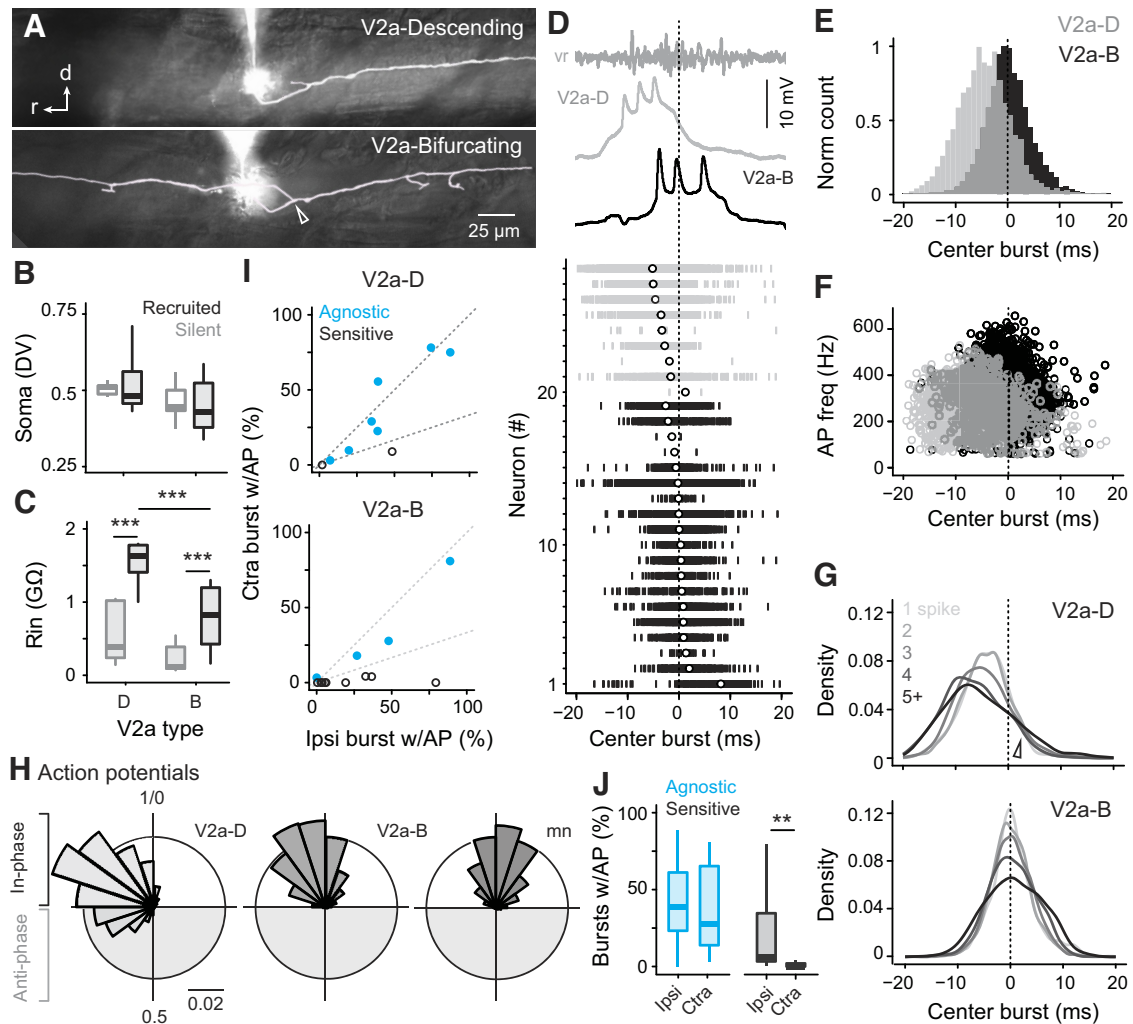


Figure 5. Anatomically distinct V2a subsets are direction sensitive and direction agnostic. **A**, Lateral views of two morphologically distinct types of V2a interneurons. Descending V2as (V2a-Ds; top) have an exclusively descending axon while bifurcating V2as (V2a-Bs; bottom) have a descending and ascending axon (bifurcation point at open arrowhead). Axon reconstructions are superimposed on composite fluorescence/differential interference contrast images collected *post hoc*. Dorsal is up, and rostral is to the left. **B**, Box-and-whisker plots of dorsoventral somata locations of silent (gray; $n = 9$ V2a-D; $n = 15$ V2a-B) and recruited (black; $n = 11$ V2a-D; $n = 16$ V2a-B) V2a interneurons; 0 and 1 signify the ventral and dorsal boundary, respectively. No significant differences were observed between silent and recruited V2a-D (Wilcoxon rank-sum test, $W = 426$, $p > 0.05$) or V2a-B interneurons (Wilcoxon rank-sum test, $W = 1583$, $p > 0.05$). **C**, Box-and-whisker plots of input resistances of silent (gray; $n = 10$ V2a-D; $n = 16$ V2a-B) and recruited (black; $n = 10$ V2a-D; $n = 14$ V2a-B) V2a interneurons. Significant differences were observed between silent and recruited V2a-D (Wilcoxon rank-sum test, $W = 350$, $p < 0.001$) and between silent and recruited V2a-B interneurons (Wilcoxon rank-sum test, $W = 1583$, $p < 0.001$). **D**, Raster plot showing the timing of spikes from all recruited V2a interneurons (bottom) relative to the center of nearby ventral rootlet activity. Each row represents action potentials (tick marks) from the same V2a interneuron across all recorded ipsilateral and contralateral trials. Open circles are median values. V2a-Ds are shaded gray, and V2a-Bs are shaded black. Top trace, An example of V2a-D (gray) and V2a-B (black) recruitment aligned to the center of nearby ventral rootlet activity. **E**, Normalized histograms of spike timing relative to the center of nearby ventral rootlet activity for V2a-D (gray; $n = 4812$ spikes) and V2a-B (black; $n = 8346$ spikes) neurons. **F**, As in **E**, but with spike timing relative to center burst versus instantaneous spike frequency for V2a-D (gray) and V2a-B (black) neurons. **G**, As in **E**, but spike densities partitioned by the number of spikes per burst for V2a-D (top) and V2a-B (bottom) neurons. Open arrowhead marks a dip in spike densities in the second half of the burst. **H**, Binned polar-phase plots of V2a-D (left), V2a-B (middle), and motor neuron (mn; right) recruitment activity. Counts are normalized to the total number of spikes recorded in each condition. V2a-D recruitment occurs before V2a-B and motor neuron recruitment. V2a-B interneurons are also recruited before motor neurons. **I**, Scatter plot of average recruitment probability, defined as number of motor bursts with action potentials (APs) over the total number of observed motor bursts, during ipsilateral (Ipsi burst w/AP) and contralateral (Ctra burst w/AP) turns for direction-sensitive (open black circle) and direction-agnostic (blue circle) V2a neurons. Dashed lines indicate unity and the boundary for distinguishing direction-agnostic and sensitive neurons. **J**, Box-and-whisker plots of the percentage of bursts accompanied by a V2a, which fired an action potentials for direction-agnostic (blue) and direction-sensitive (black) populations. The direction-sensitive population was significantly more active during ipsilateral than contralateral turns (Wilcoxon rank-sum test, $W = 14$, $p < 0.01$). No significant difference was observed in the direction-agnostic population (Wilcoxon rank-sum test, $W = 52$, $p > 0.05$). Asterisks indicate significance level; * $p < 0.05$; ** $p < 0.01$; *** $p < 0.001$.

distinct morphologic classes linked to their functions (Menelaou et al., 2014; Song et al., 2018; Menelaou and McLean, 2019; Pallucchi et al., 2022). V2a neurons with ipsilateral descending axons are thought to provide higher-order timing signals, while V2a neurons with ipsilateral bifurcating axons provide last-order regulation of motor output intensity (Menelaou and McLean, 2019). To target V2a neurons for whole-cell patch-clamp recording, we used Tg[CHX10:GFP] larvae and

confirmed their descending ($n = 14$ cells) or bifurcating ($n = 21$ cells) axon morphology *post hoc* (Fig. 5A). This allowed us to link morphology to differences in activity patterns during directed swimming triggered by drifting stimuli.

We first assessed differences in the dorsoventral soma position and the input resistance of V2a neurons recruited during directed swimming, since these features have been linked to V2a recruitment order in the past (McLean et al., 2007). We observed

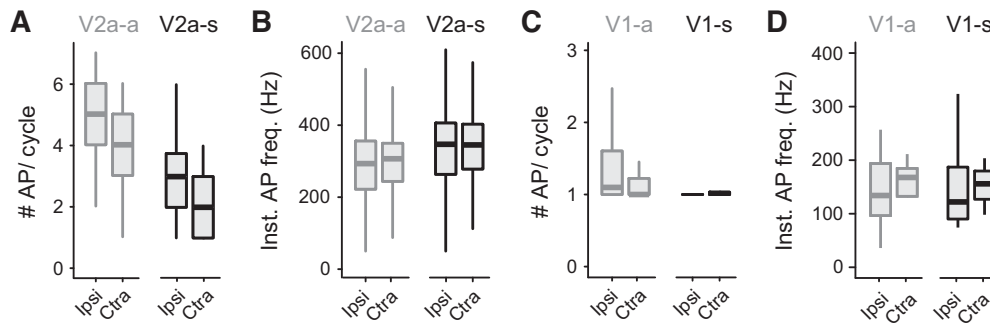


Figure 6. V2a and V1 instantaneous spike frequencies are not modulated by turn direction. **A**, Box-and-whisker plot of the mean number of action potentials per cycle for recruited cycles only for direction-agnostic V2a interneurons (V2a-as; Wilcoxon rank-sum test, $W = 26$, $p > 0.05$) and direction-selective V2a interneurons (V2a-ss; Wilcoxon rank-sum test, $W = 4$, $p > 0.05$). **B**, Box-and-whisker plot of instantaneous action potential frequency during recruited bursts for V2a-a (Wilcoxon rank-sum test, $W = 36$, $p > 0.05$) and V2a-s (Wilcoxon rank-sum test, $W = 125$, $p > 0.05$) V2a interneurons. **C**, Box-and-whisker plot of the mean number of action potentials per cycle for recruited cycles only for direction-agnostic V1 interneurons (V1-a; Wilcoxon rank-sum test, $W = 122$, $p > 0.05$) and direction-selective V1 interneurons (V1-s; Wilcoxon rank-sum test, $W = 8$, $p > 0.05$). **D**, Box-and-whisker plot of instantaneous action potential frequency during recruited bursts for the V1-a (Wilcoxon rank-sum test, $W = 42$, $p > 0.05$) and V1-s (Wilcoxon rank-sum test, $W = 26$, $p > 0.05$) subgroups.

no significant differences in soma position that predicted whether they were recruited during directed swimming for either descending or bifurcating V2a neurons (Fig. 5B). However, for both types of V2a neurons, neurons with higher input resistances were more likely to be recruited (Fig. 5C). Between the recruited types, descending V2a neurons had higher input resistances than bifurcating V2a neurons (Fig. 5C). This relationship is consistent with studies of descending and bifurcating V2a neurons recruited during higher-frequency escape swimming (Menelaou and McLean, 2019) whose lower input resistances overlap with the silent V2a neurons.

Next, we normalized the relative timing of spikes to the center of motor bursts and observed a clear difference in spike timing as a function of morphology. Descending V2a neurons were recruited earlier than bifurcating neurons (Figs. 4E, 5D), commensurate with an earlier peak in instantaneous spike frequencies (Fig. 5F). Increases in the number of spikes per cycle in descending V2a neurons were characterized by an earlier peak in spike densities relative to center burst (Fig. 5G, top), with a consistent dip ~ 5 ms after center burst (Fig. 5G, arrow). On the other hand, spike timing within the bifurcating V2a neuron population more closely resembled motor neuron spiking, with a symmetrical broadening in spike distribution and peak densities aligned to center burst (Fig. 5G, bottom). Differences in the distribution of spikes were also observed when spiking was normalized to phase (Fig. 5H). Specifically, spiking in descending V2a neurons was significantly advanced compared with bifurcating V2a neurons (Watson's test, $U = 39.8$, $p < 0.001$) and motor neurons (Watson's test, $U = 194$, $p < 0.001$), while bifurcating V2a neurons fired significantly in advance of motor neurons (Watson's test, $U = 350$, $p < 0.001$). In addition, the phasic distribution of spiking in both types of V2a neurons was statistically indistinguishable from phasic EPSC distributions in motor neurons (Fig. 4E; Watson's test, $U = 0.11$, $p > 0.05$).

Critically, when we examined V2a recruitment probability, bifurcating V2a neurons were more likely to be sensitive to the directionality of the turn ($n = 9$ of 13), whereas the majority of descending V2a neurons ($n = 7$ of 9) were direction agnostic (Fig. 5I). When we divided the V2a population into direction-sensitive and direction-agnostic subtypes, this revealed a significant increase in recruitment probability among direction-sensitive V2a neurons only (Fig. 5J), which matched increases in recruitment probabilities found in direction-sensitive motor neurons (Fig. 2F). However, the number of spikes per burst was not

significantly modulated in either subtype (Fig. 6A), nor was there any modulation of instantaneous firing frequency related to turn direction (Fig. 6B).

These observations are consistent with the idea that descending V2a neurons are upstream from bifurcating V2a neurons and are principally concerned with the timing of motor activity across and along the body, while bifurcating V2a neurons are primarily recruited on the ipsilateral side to increase the recruitment probability of motor neurons to control direction.

V1 neurons are divided into turn direction-sensitive and direction-agnostic subsets

Next, we explored the most likely source of increased in-phase premotor inhibition observed during directed swimming responses. Ipsilaterally projecting En1-labeled inhibitory V1 interneurons are a major source of premotor in-phase inhibition and have been implicated in regulating the timing of motor activity and the duration of motor bursts (Gosgnach et al., 2006; Falgairolle and O'Donovan, 2019; Kimura and Higashijima, 2019). Unlike V2a neurons, thus far there is no evidence of morphologically distinct subsets in larval zebrafish (Higashijima et al., 2004a; Kimura and Higashijima, 2019; Sengupta et al., 2021), with all V1 neurons characterized by a long ascending axon and a shorter descending one (Fig. 7A). Therefore, we pooled all V1 recordings for analysis.

We first assessed the timing of V1 spiking relative to the center of the motor burst. Almost all median values were distributed after the center burst (Fig. 7B), which was also reflected in histograms of spike counts (Fig. 7C) and peak firing frequencies (Fig. 7D). Increases in spike number per burst were also associated with a symmetrical broadening of spike distribution, with peak values well aligned regardless of spike number (Fig. 7E). Notably, the peak in firing occurred ~ 5 ms from center burst (Fig. 7E), consistent with the dips in firing observed in motor neurons (Fig. 2K) and descending V2a neurons (Fig. 5G). Differences in the timing of spikes were observed when normalized to phase, with the distribution of V1 activity trailing spiking in motor neurons (Fig. 7F); however, this was not significantly different (Watson's test, $U = 0.2$, $p > 0.05$).

Since V2a neurons could be divided into turn direction-sensitive and direction-agnostic subsets, we were curious whether the same pattern might also be observed among V1 neurons. Since we could not rely on morphology to distinguish different types, we instead plotted the percentage of bursts with spikes on the opposite side of the turn (ctra) versus that on the same side (ipsi), with

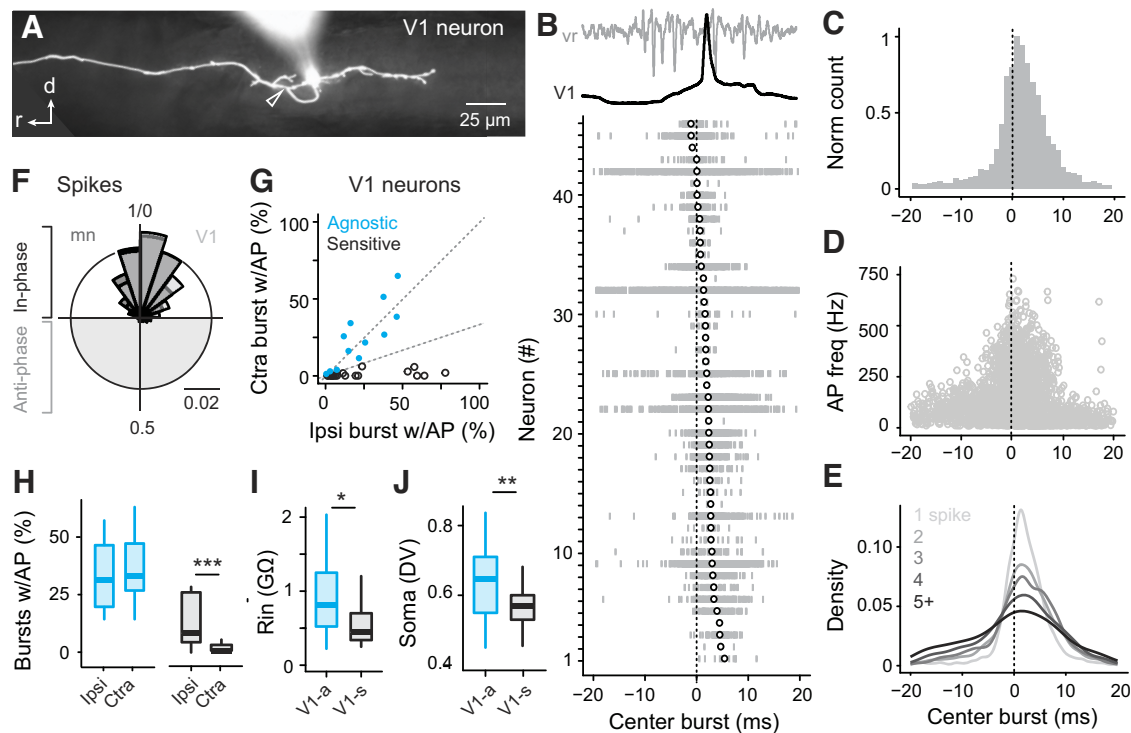


Figure 7. Inhibitory V1 neuron recruitment patterns. **A**, Lateral view of a V1 interneuron with a short descending axon branch bifurcating from the ascending branch (open arrowhead). Axon reconstruction is superimposed on a composite fluorescence/differential interference contrast image collected *post hoc*. Dorsal is up, and rostral is to the left. **B**, Raster plot showing the timing of action potentials from all recruited V1 interneurons (bottom) relative to the center of nearby ventral rootlet activity. Each row represents action potentials (tick marks) from the same V1 interneuron across all recorded ipsilateral and contralateral trials. Open circles are median values. Top trace, An example of V1 recruitment (black) aligned to the center of nearby ventral rootlet activity (gray). **C**, Normalized histogram of spike timing ($n = 5436$ spikes) relative to the center of nearby ventral rootlet activity for V1s. **D**, As in **C**, but spike densities for V1s partitioned by the number of spikes per burst. **E**, Binned polar-phase plots of V1 interneuron spiking (light gray) superimposed on motor neuron spiking (dark gray). Counts are normalized to the total number of spikes. There was no significant difference in distributions. **F**, Scatter plot of average recruitment probability during ipsi and contralateral (Ctra) turns for direction-sensitive (black, $n = 20$ cells) and direction-agnostic (blue, $n = 13$ cells) V1 interneurons. Dashed lines, Unity and the boundary for distinguishing direction-agnostic and direction-sensitive neurons. **G**, Box-and-whisker plots of recruitment probability for direction-agnostic (blue) and direction-sensitive (black) V1 interneurons. Direction-sensitive V1 interneurons were significantly more recruited during ipsilateral gratings (Wilcoxon signed-rank test, $V = 4$, $p < 0.001$), while there was no significant difference for direction-agnostic V1 interneurons (Wilcoxon signed-rank test, $V = 31$, $p > 0.05$). **H**, Box-and-whisker plot of input resistances ($G\Omega$) of direction-sensitive (blue) and direction-agnostic (black) V1 interneurons. A significant difference in resistances was observed between direction-agnostic and direction-sensitive V1 interneurons (Wilcoxon rank-sum test, $W = 37$, $p < 0.05$). **I**, Box-and-whisker plots of dorsoventral (DV) soma position of direction-sensitive (blue) and direction-agnostic (black) V1 interneurons. A significant difference in DV position was observed between the two populations (Wilcoxon rank-sum test, $W = 24$, $p < 0.01$). Asterisks indicate significance level; * $p < 0.05$; ** $p < 0.001$; *** $p < 0.0001$.

the expectation that direction-sensitive V1 neurons would deviate from unity using the same criterion as motor neuron and V2a populations (Fig. 7G). This divided the population into direction-sensitive (V1-s) and direction-agnostic V1 neurons (V1-a) categories (Fig. 7H). Analysis of input resistance (Fig. 7I) and dorsoventral soma position (Fig. 7J) revealed that direction-sensitive V1 neurons had significantly lower resistances and had more ventral soma positions. However, we observed no significant differences in spike distributions relative to center burst between the V1-a and V1-s subsets as we observed for V2a neurons (Watson's test, $U = 1.71$, $p > 0.05$). In addition, there was no significant modulation of spikes per burst (Fig. 6C) or instantaneous spike frequency (Fig. 6D) related to turn direction or subtype.

These data suggest that V1 neurons are also organized into turn direction-sensitive and direction-agnostic subsets, with direction-sensitive V1 neurons likely contributing to increased in-phase inhibition on the turning side reported in voltage-clamp recordings.

Discussion

Previous connectivity studies of spinal interneurons in tadpoles and lampreys have delineated excitatory and inhibitory interactions within a central pattern generator (CPG; Fig. 8A)

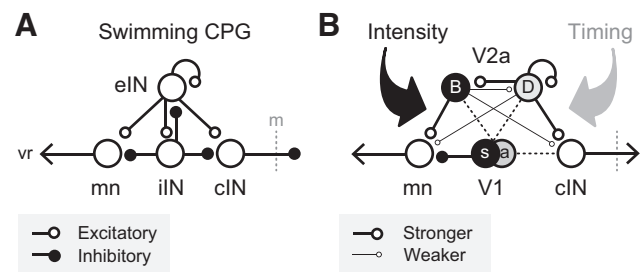


Figure 8. Spinal circuit diagrams for swimming. **A**, In the canonical lamprey and tadpole swimming CPG, there are connections from V2a-like excitatory interneurons (eINs) to motor neurons (mns), to V1-like inhibitory interneurons [ipsilateral inhibitory interneurons (iINs)], and to commissural inhibitory interneurons (cINs), which cross the midline (m) and maintain left-right alternation via reciprocal inhibition. vr, Ventral rootlet. **B**, In zebrafish, we find that V2a neurons can be characterized as heterogeneous, with V2a neurons divided anatomically into descending (D) and bifurcating (B) subtypes with direction-sensitive and direction-agnostic properties. We find here that V1 neurons are also heterogeneous, divided into direction-sensitive (s) and direction-agnostic (a) subsets. Dashed lines indicate published connectivity between V1 and V2a neurons (Kimura and Higashijima, 2019; Sengupta et al., 2021) and connections from V1 neurons to cINs (Sengupta et al., 2021) that have yet to be linked to direction-sensitive and agnostic subsets.

responsible for timing and intensity control during swimming (Buchanan and Grillner, 1987, 1988; Li et al., 2004). However, it is challenging to use this model to explain adjustments in intensity without impacting timing. In more recent connectivity studies mapping molecularly defined populations in larval and adult zebrafish onto canonical CPG types (Higashijima et al., 2004b; Bhatt et al., 2007; Song et al., 2018; Menelaou and McLean, 2019; Sengupta et al., 2021), it has been suggested that timing and intensity are controlled by distinct types. By using visual stimuli to alter the direction of locomotion while recording from spinal neurons, we tested the theory that spinal interneurons provide modular control of movement timing and intensity. In support, we find that Chx10-labeled V2a neurons are composed of direction-agnostic, largely descending subtypes for timing control and direction-sensitive, largely bifurcating subtypes for intensity control. En1-labeled V1 neurons are also divided into direction-agnostic and direction-sensitive modules, although the links to morphology are not as clear as they are among V2a neurons (Fig. 8B).

Origins of asymmetric motor output

Directed swimming is accomplished by unilateral increases in the duration of motor bursts leading to longer duty cycles. This could reflect not only an increase in the active motor pool, but also desynchronized motor neuron spiking activity (Zhang et al., 2009), more spikes per cycle (Sillar et al., 1992) or higher rates of firing (Hoffer et al., 1987) within the active pool. At the low swimming frequencies evoked here during fictive optomotor responses, recruitment probabilities for fast and slow motor neurons were relatively low, albeit more likely in slow units as expected (McLean et al., 2007). Among recruited units, we found no significant difference in spike number or rate associated with a unilateral increase in motor output. Similarly, there was no variation in the synchronization since all spikes were aligned to the center of the motor burst regardless of burst duration and spike number. Instead, we find that increases in duty cycles primarily reflect increased recruitment of fast and slow motor units that have the capacity to fire multiple spikes per burst when activated. More spikes per burst would provide more reliable activation of fast and slow muscle fibers on the turning side and stronger contractions to adjust direction (Wang and Brehm, 2017). Notably, not all fast and slow units were direction sensitive, suggesting that turning signals are not uniformly distributed within the motor pool.

Our voltage-clamp recordings from motor neurons revealed that increases in recruitment probability on the turning side are associated with increases in excitation in 28 of 34 recordings (80%) and with inhibition arriving in phase in 14 of 28 recordings (50%). These observations are relatively consistent with the fraction of direction-sensitive motor units (~70%), again suggesting that excitatory and inhibitory direction signals are not uniformly distributed throughout the pool. The recruitment of new V2a and V1 circuitry on the turning side is most likely responsible for in-phase increases in EPSCs and IPSCs, which ultimately drive unilateral increases in motor output. For V2a neurons, recruitment of primarily bifurcating subtypes translates into recruitment of motor neurons. As with motor neurons, we found no significant difference in spike number or rate related to turning. This contrasts recordings of bifurcating V2a neurons recruited during escape turns, where unilateral differences in turn intensity are encoded by differences in spike rate with 100% recruitment (Bhatt et al., 2007). During lower-velocity optomotor

responses bifurcating V2a neuron recruitment rarely exceeds 25% per cycle. This is comparable to recruitment probabilities in direction-sensitive motor neurons and likely reflects the relatively subtle direction adjustments during optomotor responses compared with escapes.

For both types of V1 neurons, spike distributions peak just after burst center, consistent with a role in terminating local motor bursts, which are longer on the turning side. V1 neurons also fire during the motor burst, suggesting that they could also play a role in gain control by shaping motor neuron recruitment on the turning side, as suggested for V1-derived Renshaw neurons in mammalian spinal cord (Renshaw, 1946; Eccles et al., 1954, 1961; Windhorst, 1996; Hultborn et al., 2004; Alvarez and Fyffe, 2007). Direction-sensitive V1 neurons also rarely exceeded 25% recruitment reliabilities on the turning side, consistent with motor neuron and V2a neuron data. This also suggests at this speed the impact of V1 activity on motor neuron firing is relatively subtle. In contrast, EPSCs and IPSCs arriving antiphase on the turning side are not impacted significantly by turn direction, suggesting they arise from direction-agnostic circuits on the opposite side of spinal cord. This could include commissural excitatory V0v interneurons and inhibitory V0d interneurons or dI6 interneurons (Satou et al., 2012; Kishore et al., 2020). It remains to be seen how these spinal populations may also distribute the control of timing versus intensity.

Functional modularity of V2a and V1 neurons

To assess the contribution of the spinal locomotor circuitry to asymmetric adjustments in phasic premotor drive and motor output, we focused on V2a neurons that provide in-phase premotor excitation in zebrafish and mice (Kimura et al., 2006; McLean et al., 2008; Dougherty and Kiehn, 2010; Eklöf-Ljunggren et al., 2012; Zhong et al., 2012; Ampatzis et al., 2014; Menelaou and McLean, 2019). Descending V2a neurons fired reliably on the turning and nonturning sides, consistent with a primary role in ensuring the maintenance of motor coordination along and across the body regardless of direction of travel. Descending V2a neurons were also rhythmically active in advance of bifurcating V2a neurons and motor neurons, as expected for rhythm-generating neurons (Buchanan and Grillner, 1987). In addition, increases in spike number per burst in descending V2a neurons were not symmetrically distributed around the center of the motor burst, as they were for bifurcating V2a neurons and motor neurons. This suggests descending V2a neurons are upstream from the timing signals that ensure symmetrical spike distributions or are responsible for generating them.

Bifurcating V2a neurons fired more reliably on the turning side, making them good candidates for unilateral increases in motor neuron recruitment during turns. In addition, the peak distribution of phasic spikes in bifurcating V2a neurons fell between descending V2a neurons and motor neurons, suggesting they are relaying information to motor neurons. Their position downstream of rhythm-generating circuits makes them ideally suited to integrate locomotor-related and direction signals. If descending spinal V2a neurons provide rhythmic drive to bifurcating V2a neurons (Menelaou and McLean, 2019), then directional signals could arise from reticulospinal inputs (Orger et al., 2008; Huang et al., 2013; Pujala and Koyama, 2019).

The directed swimming we evoked here is characterized by lower swimming frequencies and so the more reliable participation of higher input resistance, slow motor units we observed is consistent with previous work (McLean et al., 2007). For V2a and V1 interneurons, direction-agnostic subtypes had the highest

input resistances, suggesting a similar link between excitability and function. The current view is that zebrafish V2a neurons in the spinal cord and brainstem form frequency-specific modules related to their innervation of fast, intermediate, and slow motor units (Song et al., 2018, 2020; Pujala and Koyama, 2019). While fast motor units fire less reliably at the low burst frequencies observed during fictive optomotor responses, we find they receive phasic excitatory drive and their temporal distribution of spikes is indistinguishable from slow units. Thus, some form of short-latency, cross-module frequency integration must exist, but has yet to be revealed.

Our recordings from V1 neurons also revealed distinct functional, if not morphologic, subtypes based on their characterization as direction-agnostic and direction-sensitive. In larval zebrafish, V1 neurons have been implicated in prematurely terminating and/or silencing spiking in V2a neurons to regulate motor burst frequency and also in regulating the duration of motor bursts to control duty cycle (Kimura and Higashijima, 2019; Sengupta et al., 2021). Our work suggests that these functions are conducted by distinct V1 modules. The division of timing and intensity control resembles observations in mice, where the V1 population includes Ia inhibitory interneurons controlling flexor–extensor timing and Renshaw cells controlling the gain of motor output (Goulding et al., 2014). Moreover, genetic ablation of the entire V1 population has a similar impact on the timing and intensity of motor output reported in zebrafish (Gosgnach et al., 2006; Kimura and Higashijima, 2019).

Broader impact

The idea that fish have modular control of timing and intensity is analogous to the idea proposed in mammalian spinal locomotor networks “rhythm-generating” interneurons control timing and subordinate “pattern-forming” interneurons control intensity (Rybak et al., 2006). In mice, modular control of rhythm and pattern is thought to simplify adjustments in response to sensory stimuli and the production of different gaits (Dougherty and Ha, 2019). Here, we find that for optomotor responses in zebrafish, adjustments in intensity occur without changes in timing. However, reorientation maneuvers that involve adjustments in timing have previously been observed during strong evasive stimuli in fish (Svoboda and Fetcho, 1996; McClellan and Hagevik, 1997; Fagerstedt et al., 2001; Fagerstedt and Ullén, 2001). One possibility is that evasive stimuli have access to direction-agnostic V2a and V1 neurons to alter timing. Another possibility worth exploring is that more reliable recruitment of direction-sensitive V2a and V1 neurons can alter timing.

Ultimately, our findings support the notion that shared circuit motifs underly locomotor control in vertebrates. The utility of spinal modular control of timing and intensity in zebrafish likely simplifies smooth adjustments in orientation while on the move. This sets the stage for a better understanding of how descending control systems rely on and exploit spinal circuit dynamics to navigate effectively.

References

- Alvarez FJ, Fyffe REW (2007) The continuing case for the Renshaw cell. *J Physiol* 584:31–45.
- Ampatzis K, Song J, Ausborn J, El Manira A (2014) Separate microcircuit modules of distinct V2a interneurons and motoneurons control the speed of locomotion. *Neuron* 83:934–943.
- Ausborn J, Mahmood R, El Manira A (2012) Decoding the rules of recruitment of excitatory interneurons in the adult zebrafish locomotor network. *Proc Natl Acad Sci U S A* 109:E3631–E3639.
- Bagnall MW, McLean DL (2014) Modular organization of axial microcircuits in zebrafish. *Science* 343:197–200.
- Balciunas D, Davidson AE, Sivasubbu S, Hermanson SB, Welle Z, Ekker SC (2004) Enhancer trapping in zebrafish using the *Sleeping Beauty* transposon. *BMC Genomics* 5:62.
- Bello-Rojas S, Istrate AE, Kishore S, McLean DL (2019) Central and peripheral innervation patterns of defined axial motor units in larval zebrafish. *J Comp Neurol* 527:2557–2572.
- Bhatt DH, McLean DL, Hale ME, Fetcho JR (2007) Grading movement strength by changes in firing intensity versus recruitment of spinal interneurons. *Neuron* 53:91–102.
- Bhattacharyya K, McLean DL, MacIver MA (2017) Visual threat assessment and reticulospinal encoding of calibrated responses in larval zebrafish. *Curr Biol* 27:2751–2762.e6.
- Bianco IH, Kampff AR, Engert F (2011) Prey capture behavior evoked by simple visual stimuli in larval zebrafish. *Front Syst Neurosci* 5:101.
- Buchanan JT, Grillner S (1987) Newly identified “glutamate interneurons” and their role in locomotion in the lamprey spinal cord. *Science* 236:312–314.
- Buchanan JT, Grillner S (1988) A new class of small inhibitory interneurons in the lamprey spinal cord. *Brain Res* 438:404–407.
- Burgess HA, Schoch H, Granato M (2010) Distinct retinal pathways drive spatial orientation behaviors in zebrafish navigation. *Curr Biol* 20:381–386.
- Buss RR, Drapeau P (2001) Synaptic drive to motoneurons during fictive swimming in the developing zebrafish. *J Neurophysiol* 86:197–210.
- Chen X, Engert F (2014) Navigational strategies underlying phototaxis in larval zebrafish. *Front Syst Neurosci* 8:39.
- Dougherty KJ, Ha NT (2019) The rhythm section: an update on spinal interneurons setting the beat for mammalian locomotion. *Curr Opin Physiol* 8:84–93.
- Dougherty KJ, Kiehn O (2010) Firing and cellular properties of V2a interneurons in the rodent spinal cord. *J Neurosci* 30:24–37.
- Dougherty KJ, Zagoraiou L, Satoh D, Rozani I, Doobar S, Arber S, Jessell TM, Kiehn O (2013) Locomotor rhythm generation linked to the output of spinal Shox2 excitatory interneurons. *Neuron* 80:920–933.
- Dunn TW, Gebhardt C, Naumann EA, Riegler C, Ahrens MB, Engert F, Del Bene F (2016) Neural circuits underlying visually evoked escapes in larval zebrafish. *Neuron* 89:613–628.
- Eccles JC, Fatt P, Koketsu K (1954) Cholinergic and inhibitory synapses in a pathway from motor-axon collaterals to motoneurons. *J Physiol* 126:524–562.
- Eccles JC, Eccles RM, Iggo A, Ito M (1961) Distribution of recurrent inhibition among motoneurons. *J Physiol* 159:479–499.
- Eklöf-Ljunggren E, Haupt S, Ausborn J, Dehnisch I, Uhlén P, Higashijima S, El Manira A (2012) Origin of excitation underlying locomotion in the spinal circuit of zebrafish. *Proc Natl Acad Sci U S A* 109:5511–5516.
- Fagerstedt P, Ullén F (2001) Lateral turns in the lamprey. I. Patterns of motoneuron activity. *J Neurophysiol* 86:2246–2256.
- Fagerstedt P, Orlovsky GN, Deliaquina TG, Grillner S, Ullén F (2001) Lateral turns in the lamprey. II. Activity of reticulospinal neurons during the generation of fictive turns. *J Neurophysiol* 86:2257–2265.
- Falgairolle M, O'Donovan MJ (2019) V1 interneurons regulate the pattern and frequency of locomotor-like activity in the neonatal mouse spinal cord. *PLoS Biol* 17:e3000447.
- Gosgnach S, Lanuza GM, Butt SJB, Saueressig H, Zhang Y, Velasquez T, Riethmacher D, Callaway EM, Kiehn O, Goulding M (2006) V1 spinal neurons regulate the speed of vertebrate locomotor outputs. *Nature* 440:215–219.
- Goulding M (2009) Circuits controlling vertebrate locomotion: moving in a new direction. *Nat Rev Neurosci* 10:507–518.
- Goulding M, Bourane S, Garcia-Campmany L, Dalet A, Koch S (2014) Inhibition downunder: an update from the spinal cord. *Curr Opin Neurobiol* 26:161–166.
- Grillner S, El Manira A (2020) Current principles of motor control, with special reference to vertebrate locomotion. *Physiol Rev* 100:271–320.
- Guan NN, Xu L, Zhang T, Huang CX, Wang Z, Dahlberg E, Wang H, Wang F, Pallucchi I, Hua Y, El Manira A, Song J (2021) A specialized spinal circuit for command amplification and directionality during escape behavior. *Proc Natl Acad Sci U S A* 118:e2106785118.
- Ha NT, Dougherty KJ (2018) Spinal shox2 interneuron interconnectivity related to function and development. *Elife* 7:e42519.

- Higashijima S-I, Masino MA, Mandel G, Fetcho JR (2004a) Engrailed-1 expression marks a primitive class of inhibitory spinal interneuron. *J Neurosci* 24:5827–5839.
- Higashijima S-I, Mandel G, Fetcho JR (2004b) Distribution of prospective glutamatergic, glycinergic, and GABAergic neurons in embryonic and larval zebrafish. *J Comp Neurol* 480:1–18.
- Hoffer JA, Sugano N, Loeb GE, Marks WB, O'Donovan MJ, Pratt CA (1987) Cat hindlimb motoneurons during locomotion. II. Normal activity patterns. *J Neurophysiol* 57:530–553.
- Huang K-H, Ahrens MB, Dunn TW, Engert F (2013) Spinal projection neurons control turning behaviors in zebrafish. *Curr Biol* 23:1566–1573.
- Hultborn H, Brownstone RB, Toth TI, Gossard JP (2004) Key mechanisms for setting the input-output gain across the motoneuron pool. *Prog Brain Res* 143:75–95.
- Kiehn O (2016) Decoding the organization of spinal circuits that control locomotion. *Nat Rev Neurosci* 17:224–238.
- Kimura Y, Higashijima S (2019) Regulation of locomotor speed and selection of active sets of neurons by V1 neurons. *Nat Commun* 10:2268.
- Kimura Y, Okamura Y, Higashijima S-i (2006) *alk*, a zebrafish homolog of *Chx10*, marks ipsilateral descending excitatory interneurons that participate in the regulation of spinal locomotor circuits. *J Neurosci* 26:5684–5697.
- Kishore S, Cadoff EB, Agha MA, McLean DL (2020) Orderly compartmental mapping of premotor inhibition in the developing zebrafish spinal cord. *Science* 370:431–436.
- Kleiner M, Brainerd DH, Pelli DG, Ingling A, Murray R, Broussard C (2007) What's new in psychtoolbox-3. *Perception* 36:1–16.
- Li WC, Higashijima SI, Parry DM, Roberts A, Soffe SR (2004) Primitive roles for inhibitory interneurons in developing frog spinal cord. *J Neurosci* 24:5840–5848.
- McClellan AD, Hagevik A (1997) Descending control of turning locomotor activity in larval lamprey: neurophysiology and computer modeling. *J Neurophysiol* 78:214–228.
- McElligott MB, O'Malley DM (2005) Prey tracking by larval zebrafish: axial kinematics and visual control. *Brain Behav Evol* 66:177–196.
- McLean DL, Fetcho JR (2009) Spinal interneurons differentiate sequentially from those driving the fastest swimming movements in larval zebrafish to those driving the slowest ones. *J Neurosci* 29:13566–13577.
- McLean DL, Fan J, Higashijima S, Hale ME, Fetcho JR (2007) A topographic map of recruitment in spinal cord. *Nature* 446:71–75.
- McLean DL, Masino MA, Koh IYY, Lindquist WB, Fetcho JR (2008) Continuous shifts in the active set of spinal interneurons during changes in locomotor speed. *Nat Neurosci* 11:1419–1429.
- Menelaou E, McLean DL (2012) A gradient in endogenous rhythmicity and oscillatory drive matches recruitment order in an axial motor pool. *J Neurosci* 32:10925–10939.
- Menelaou E, McLean DL (2019) Hierarchical control of locomotion by distinct types of spinal V2a interneurons in zebrafish. *Nat Commun* 10:4197.
- Menelaou E, VanDunk C, McLean DL (2014) Differences in the morphology of spinal V2a neurons reflect their recruitment order during swimming in larval zebrafish. *J Comp Neurol* 522:1232–1248.
- Myers P, Eisen J, Westerfield M (1986) Development and axonal outgrowth of identified motoneurons in the zebrafish. *J Neurosci* 6:2278–2289.
- Neuhaus SCF, Biehlmaier O, Seeliger MW, Das T, Kohler K, Harris WA, Baier H (1999) Genetic disorders of vision revealed by a behavioral screen of 400 essential loci in zebrafish. *J Neurosci* 19:8603–8615.
- Orger MB, Kampff AR, Severi KE, Bollmann JH, Engert F (2008) Control of visually guided behavior by distinct populations of spinal projection neurons. *Nat Neurosci* 11:327–333.
- Pallucchi I, Bertuzzi M, Michel JC, Miller AC, El Manira A (2022) Transformation of an early-established motor circuit during maturation in zebrafish. *Cell Rep* 39:110654.
- Patterson BW, Abraham AO, MacIver MA, McLean DL (2013) Visually guided gradation of prey capture movements in larval zebrafish. *J Exp Biol* 216:3071–3083.
- Perkins KL (2006) Cell-attached voltage-clamp and current-clamp recording and stimulation techniques in brain slices. *J Neurosci Methods* 154:1–18.
- Portugues R, Engert F (2011) Adaptive locomotor behavior in larval zebrafish. *Front Syst Neurosci* 5:72.
- Pujala A, Koyama M (2019) Chronology-based architecture of descending circuits that underlie the development of locomotor repertoire after birth. *Elife* 8:e42135.
- Renshaw B (1946) Central effects of centripetal impulses in axons of spinal ventral roots. *J Neurophysiol* 9:191–204.
- Roberts A, Li WC, Soffe SR (2010) How neurons generate behavior in a hatchling amphibian tadpole: an outline. *Front Behav Neurosci* 4:16.
- Roeser T, Baier H (2003) Visuomotor behaviors in larval zebrafish after GFP-guided laser ablation of the optic tectum. *J Neurosci* 23:3726–3734.
- Rybak IA, Shevtsova NA, Lafreniere-Roula M, McCrea DA (2006) Modelling spinal circuitry involved in locomotor pattern generation: insights from deletions during fictive locomotion. *J Physiol* 577:617–639.
- Satou C, Kimura Y, Higashijima S (2012) Generation of multiple classes of V0 neurons in zebrafish spinal cord: progenitor heterogeneity and temporal control of neuronal diversity. *J Neurosci* 32:1771–1783.
- Sengupta M, Daliparthi V, Roussel Y, Bui TV, Bagnall MW (2021) Spinal V1 neurons inhibit motor targets locally and sensory targets distally. *Curr Biol* 31:3820–3833.e4.
- Severi KE, Portugues R, Marques JC, O'Malley DM, Orger MB, Engert F (2014) Neural control and modulation of swimming speed in the larval zebrafish. *Neuron* 83:692–707.
- Sillar KT, Simmers AJ, Wedderburn JFS (1992) The post-embryonic development of cell properties and synaptic drive underlying locomotor rhythm generation in *Xenopus* larvae. *Proc Biol Sci* 249:65–70.
- Song J, Dahlberg E, El Manira A (2018) V2a interneuron diversity tailors spinal circuit organization to control the vigor of locomotor movements. *Nat Commun* 9:3370.
- Song J, Pallucchi I, Ausborn J, Ampatzis K, Bertuzzi M, Fontanel P, Picton LD, El Manira A (2020) Multiple rhythm-generating circuits act in tandem with pacemaker properties to control the start and speed of locomotion. *Neuron* 105:1048–1061.e4.
- Svoboda K, Fetcho J (1996) Interactions between the neural networks for escape and swimming in goldfish. *J Neurosci* 16:843–852.
- Temizer I, Donovan JC, Baier H, Semmelhack JL (2015) A visual pathway for looming-evoked escape in larval zebrafish. *Curr Biol* 25:1823–1834.
- Trivedi CA, Bollmann JH (2013) Visually driven chaining of elementary swim patterns into a goal-directed motor sequence: a virtual reality study of zebrafish prey capture. *Front Neural Circuits* 7:86.
- Wang W-C, Brehm P (2017) A gradient in synaptic strength and plasticity among motoneurons provides a peripheral mechanism for locomotor control. *Curr Biol* 27:415–422.
- Windhorst U (1996) The spinal cord and its brain: representations and models. To what extent do forebrain mechanisms appear at brainstem spinal cord levels? *Prog Neurobiol* 49:381–414.
- Zhang H-Y, Li W-C, Heitler WJ, Sillar KT (2009) Electrical coupling synchronizes spinal motoneuron activity during swimming in hatchling *Xenopus* tadpoles. *J Physiol* 587:4455–4466.
- Zhong G, Shevtsova NA, Rybak IA, Harris-Warrick RM (2012) Neuronal activity in the isolated mouse spinal cord during spontaneous deletions in fictive locomotion: insights into locomotor central pattern generator organization. *J Physiol* 590:4735–4759.